

General Disclaimer

One or more of the Following Statements may affect this Document

- This document has been reproduced from the best copy furnished by the organizational source. It is being released in the interest of making available as much information as possible.
- This document may contain data, which exceeds the sheet parameters. It was furnished in this condition by the organizational source and is the best copy available.
- This document may contain tone-on-tone or color graphs, charts and/or pictures, which have been reproduced in black and white.
- This document is paginated as submitted by the original source.
- Portions of this document are not fully legible due to the historical nature of some of the material. However, it is the best reproduction available from the original submission.

NEPTUNE: LIMB BRIGHTENING WITHIN
THE 7300 ANGSTROM METHANE BAND

Michael J. Price
Science Applications, Inc.
5055 E. Broadway, Suite A-214
Tucson, Arizona 85711

and

Otto G. Franz
Lowell Observatory
P.O. Box 1269
Flagstaff, Arizona 86002

(NASA-CR-162319) NEPTUNE: LIMB BRIGHTENING
WITHIN THE 7300 ANGSTROM METHANE BAND
(Science Applications, Inc.) 24 p
HC A02/MF A01

N79-33122

CSCL 03A

G3/89 Unclass
38204

No. of Copies: 4

No. of MS Pages: 20

No. of Figures: 5

No. of Tables: 2

ABSTRACT

Narrow-waveband (100\AA) photoelectric slit scan photometry of the Neptune disk is reported. Observations were concentrated within the strong CH_4 band at 7300\AA . For comparison, measurements were also made within a continuum waveband at 6800\AA . Point spread function data were obtained in both colors. Qualitative estimates of the true intensity distribution over the Neptune disk were made. Within the 6800\AA continuum band, Neptune appears as an essentially uniform disk. Within the 7300\AA CH_4 band, the planet exhibits strong limb-brightening. Our results appear to require the presence of an optically thin layer of brightly scattering aerosol particles high in the Neptune atmosphere.

1. INTRODUCTION

Trafton (1974) reported the first measurements of the H_2 quadrupole lines in the spectrum of Neptune. Strengths of the S(0) and S(1) lines of the (4-0) band were interpreted in terms of both an inhomogeneous atmosphere overlying a reflecting layer, and a homogeneous, semi-infinite scattering atmosphere. Only the scattering model proved to be consistent with Neptune's spectrum in this wavelength region. The H_2 abundance along a scattering mean free path was found to be ~ 320 km. amagat; the maximum permitted abundance was 450 km. amagat. By comparison, the scattering mean free path for Rayleigh scattering in a pure H_2 atmosphere is equivalent to 715 km. amagat. Although aerosol particle scattering may be responsible for the observed reduction in the mean free path, Trafton noted that an alternative explanation might be molecular scattering from gases additional to hydrogen. From an analysis of photoelectric photometry of Neptune, Lockwood (1978) concluded that the scattering properties of the atmosphere are variable, and that aerosol particles are present.

Infrared (1-4 μm) observations of Neptune have been interpreted by Joyce et al. (1977) and by Pilcher (1977) to suggest that, over a one year period, an extensive high altitude cloud formed on the planet and then partially dissipated. About 10-months after its initial appearance, the optical thickness of the cloud averaged over the planet was on the order of unity. An H_2 column-abundance of 5 ± 2 km. amagat was derived; it appeared to refer to an effective reflecting layer high in the atmosphere of Neptune.

Recent infrared (0.8 - 2.5 μm) studies of Neptune by Fink and Larson (1979) have indicated that its atmosphere has a variable height cloud layer overlain by ~ 50 km. amagat of H_2 . Fink and Larson point out that the high cloud layer cannot have a large optical thickness since both the H_2 quadrupole lines and the visible CH_4 bands give quite large abundances. Specifically, the CH_4 column abundance was found to be ~ 0.7 km. amagat. For Uranus, the corresponding value was 1.6 km. amagat. Fink and Larson also found the Uranus atmosphere to be clear to great depths with its upper

regions depleted in CH_4 . It appears likely that visible radiation can probe to great depths in the Neptune atmosphere.

Useful information concerning the opacity of the Neptune atmosphere, in particular the presence of an optically thin upper cloud layer, can be derived from measurements of the distribution of intensity over the disk of the planet both within and between the strong CH_4 bands. In this paper, we report the first attempt to infer the wavelength-dependent optical appearance of the Neptune disk.

2. OBSERVATIONS

During the 1979 Neptune apparition, narrow-band (100Å) slit scan photometry of the planet was carried out within two regions of the spectrum by the technique described by Price and Franz (1979). Scans were obtained primarily within the 7300Å CH₄ band. But, for comparison, scans were also made within the continuum region at 6800Å. Waveband selection was achieved by means of two filters used in our early investigation of Uranus (Price and Franz: 1976). On 1979 July 23, reliable observational data were obtained with the area-scanner mounted on the 1.8 meter Perkins reflector at Lowell Observatory.

Neptune was difficult to observe because of its extreme southerly declination (-21 degrees). Even at meridian transit, the planet never reached an elevation angle greater than ~ 33 degrees. In order to minimize the path length through the atmosphere, observations were restricted to within ± 2 hours of transit. Effects of differential refraction, both within and between each waveband, were avoided by orienting the slit length in a north-south direction. Both the stellar and Neptune images would then suffer dispersion along the slit when observations were made near the meridian. Special care was taken in the determination of the point spread function. A star, of apparent visual magnitude ~ 7.0, located within 45 arc. min. of Neptune, at an elevation angle essentially identical with that of the planet, was selected to provide PSF information. Both Neptune and the star were scanned in an east-west direction only. Both forward and reverse scans were used. Samples were taken at spatial intervals of 0.032 arc. sec with a slit of 100 μ m (0.645 arc. sec) width. Both slit and scan length were 2mm (12.9 arc. sec).

Each recorded scan of Neptune and of the star was obtained by integrating 100 one-second scans. Shortening the integration time, although desirable to minimize image wander produced by telescope tracking errors and by variations in atmospheric refraction, would have adversely affected the signal-to-noise ratio. If image wander did occur, we hoped to match

its effects for both Neptune and the star by equalizing their integration times. To increase the effective signal-to-noise ratio, composites of the integrated scans were subsequently computed by the method described by Price and Franz (1979). Scans made in opposite directions were mirrored on their centroids prior to computer summation. Both the Neptune and stellar composite scans were symmetrical within the level set by the residual photometric noise. Total scan numbers for both the Neptune and stellar composites are shown in Table I. Final Neptune and stellar slit scans were formed by averaging the respective composites about their centroids.

Atmospheric turbulence, together with diffuse instrumental scattering, is responsible for the observed point spread function. Our earlier investigations of Uranus (Price and Franz: 1978, 1979) showed that the point spread function is well represented by the summation of two colocated but distinct Gaussian curves. Normalizing the point spread function, $f(r)$, to unit total energy, we can write its radial distribution in the form

$$f(r) = \frac{1}{\pi [A\sigma_1^2 + B\sigma_2^2]} \left\{ A \exp [-r^2/\sigma_1^2] + B \exp [-r^2/\sigma_2^2] \right\} \quad (1)$$

where A , B , σ_1 and σ_2 are constants. Optimum sets of PSF parameters for both wavebands were obtained from the composite stellar slit scans by the method described by Price and Franz (1979). Within the 6800Å waveband, we found $A = 1$, $B = 0.1336$, $\sigma_1 = 0.9829$ arc. sec, and $\sigma_2 = 2.0730$ arc. sec. Within the 7300Å waveband, we found $A = 1$, $B = 0.1378$, $\sigma_1 = 0.9829$ arc. sec, and $\sigma_2 = 2.0413$ arc. sec. As one would expect, the point spread function became narrower with increasing wavelength. Our best-fitting analytical scans are compared with the observational data in Figures 1 and 2 for the 6800Å and 7300Å wavebands, respectively. Scaled with respect to each central intensity, the respective root mean square deviations between calculation and observation are 0.62 percent and 0.68 percent. Evidently, the goodness-of-fit in each case is limited by the residual noise in the photometric data. Stability of the point spread function during the course of the observations was high. Consider both sets of PSF data

Table I

FORMATION OF COMPOSITE STELLAR AND NEPTUNE SLIT SCANS

Waveband (Angstroms)	Scan Object	Integrated Scans	One-Second Sweeps
6800	Star	2	200
	Neptune	4	400
7300	Star	2	200
	Neptune	8	800

together. The Gaussian 1/e-widths of the individual integrated stellar slit scans exhibited an rms deviation equivalent to 2.0 percent of the mean. Residual uncertainty in the mean point spread function for each waveband will have a negligible effect on the interpretation of the planetary data.

3. ANALYSIS

Careful examination of the Neptune slit scan data showed the level of the residual photometric noise to be too high to permit reliable restoration of the actual radial intensity distribution over the disk. Instead, we chose to qualitatively investigate the appearance of the planet by comparing the observed slit scans directly with predictions made for a variety of model intensity distributions. Our approach was first to model both the size and shape of the planet and to adopt a candidate radial distribution of intensity over the disk, next to employ the known point spread function in a two-dimensional convolution to derive the planetary image smeared by atmospheric seeing, then to compute the profile which would result from slit scanning the image in one-dimension (E-W), and finally to normalize the slit scan prediction to permit comparison with the observational data. Mathematical procedures developed by Price and Franz (1978) were used.

From stellar occultation data, Freeman and Lyng⁰ (1970) found Neptune to be oblate, with an equatorial radius of 25265 ± 36 kms and an ellipticity of 0.026 ± 0.005 . Their data refer to a level in the atmosphere corresponding to a molecular number density in the range 10^{12} to 10^{13} cm^{-3} . Assuming the Neptune atmosphere to be isothermal, Freeman and Lyng⁰ derived an equatorial radius of 24753 ± 59 kms at a molecular number density of 10^{20} cm^{-3} where they expected a dense cloud layer to form. But, whether or not the Neptune atmosphere is indeed clear to such a depth is uncertain. For our present analysis, we adopted an equatorial radius of 25,000 kms. Effects of oblateness remain to be evaluated. Detailed consideration of both the observational geometry and technique showed that accurate theoretical slit scans of Neptune could be derived if the planetary disk were assumed to be perfectly circular with a radius equivalent to 0.994 times the equatorial value. Since the Neptune radius, relevant to our analysis, is not known within an accuracy of 0.5 percent, we chose to ignore the correction for oblateness. Neptune was taken to

be perfectly spherical with a radius of 25,000 kms. The American Ephemeris and Nautical Almanac gives the geocentric distance of Neptune on 1979 July 23 as 29.515 AU. The corresponding angular radius of the planet was 1.168 arc. sec.

Six simple models were adopted for the actual distribution of intensity over the Neptune disk. Circular symmetry was adopted throughout. In five models, the intensity was assumed to be a linear function of radial distance from the center of the disk. Each model was defined by the ratio of the intensities at the center and limb of the planet (CTL). A complete range of intensity distributions, from strong limb darkening through a flat disk to strong limb brightening, was considered. A sixth model represented the most extreme situation of limb brightening with the intensity assumed to be zero except within a ring of infinitesimal width located at the limb. Characteristics of the six models are summarized in Table II.

Theoretical Neptune slit scans are compared in Figure 3. All six models have been normalized to the same integrated energy. In general, the computations were based on mathematical procedures developed by Price and Franz (1978). But, for the ring of infinitesimal width, the radial intensity distribution of the smeared image was calculated by the method described in an Appendix. For both wavebands observed, the point spread functions are very similar. We therefore adopted a mean PSF for the comparison of the individual models. Specifically, its parameters were $A = 1$, $B = 0.1357$, $\sigma_1 = 0.9829$ arc. sec and $\sigma_2 = 2.0572$ arc. sec. In spite of the small angular diameter of the Neptune disk, strong limb-darkening or limb-brightening would be detectable if present. Note that the predicted scan intensity is essentially independent of the disk model at ~ 0.8 arc. sec from the profile center.

In Figures 4 and 5, observed Neptune slit scan data are compared with theoretical predictions for the 6800Å and 7300Å wavebands respectively. To avoid cluttering the diagrams, theoretical predictions are plotted only for the flat disk and for the ring of infinitesimal width. Predictions were based on the individual point spread functions relevant to each waveband. Both the observational data and theoretical predictions have

Table II

MODEL INTENSITY DISTRIBUTIONS FOR THE NEPTUNE DISK

Model	CTL
1	1:0
2	1:0.5
3	1:1
4	0.5:1
5	0:1
6	Ring

been normalized to the same integrated energy. By inspection, we conclude that Neptune is well represented by a flat disk at 6800Å, while strong limb-brightening is clearly present within the 7300Å CH₄ band. The degree of limb-brightening, however, cannot be determined accurately because of residual photometric noise.

Where the profiles are insensitive to the disk model, the observed and theoretical scans are very well matched. This consistency is most significant. It implies that tracking errors were negligible during acquisition of the Neptune data, that the radius of the planet was properly chosen, and that the observed point spread function provided an accurate description of atmospheric smearing of the disk.

4. DISCUSSION

Limb-brightening on Neptune must be the result of a vertical inhomogeneity in its atmosphere. More specifically, the single scattering albedo must decrease inversely with optical depth. Within the 7300 \AA CH_4 band, two explanations of the limb-brightening phenomenon are feasible. In the absence of aerosol particles, limb-brightening may be the result of methane depletion in the upper regions of the atmosphere. But, if the CH_4/H_2 mixing ratio is constant with optical depth, limb-brightening may be caused by an optically thin layer of aerosol particles high in the Neptune atmosphere. Hybrid explanations are also possible.

Within the 6800 \AA continuum waveband, limb-darkening would be expected to occur if the atmosphere were homogeneous. In a clear $\text{H}_2 - \text{CH}_4$ atmosphere, vibrational Raman scattering from molecular hydrogen would reduce the monochromatic single scattering albedo significantly below unity. Absorption from a weak CH_4 band at 6825 \AA would also contribute to a reduction in the single scattering albedo. Within this methane band, Giver (1978) found pressure effects to be insignificant. So no vertical inhomogeneity would result. For Neptune to appear as an essentially uniform disk, a limb-brightening mechanism must be acting to counter the natural tendency to limb-darkening. Such a mechanism could well be the presence of an optically thin layer of brightly scattering aerosol particles at high altitude. In fact, to reconcile our observational results with those obtained by other techniques, such a scattering layer appears to be essential. But whether or not the aerosol haze is laterally homogeneous cannot yet be determined.

APPENDIX

ATMOSPHERIC SMEARING OF A RING OF INFINITESIMAL WIDTH

Consider the situation of extreme limb brightening on a perfectly circular planetary disk. Suppose that all the radiation reflected by the planet is concentrated within a ring of infinitesimal width and with a radius equal to that of the disk itself. Normalizing the total radiant energy to unity, we can define the radial intensity distribution, $g(r)$, in terms of the delta function. Specifically, we can write

$$g(r) = \frac{1}{2\pi a} \delta(r - a) \quad (A-1)$$

where a is the radius of the planetary disk. Suppose further, that atmospheric turbulence produces a smear described by a circularly symmetric point spread function, $f(r)$, of the form

$$f(r) = \frac{1}{\pi [A\sigma_1^2 + B\sigma_2^2]} \cdot \left\{ A \exp [-r^2/\sigma_1^2] + B \exp [-r^2/\sigma_2^2] \right\} \quad (A-2)$$

where A , B , σ_1 and σ_2 are constants which may be determined from observational data. Convolution of the point spread function, $f(r)$, with the degenerate annulus, $g(r)$, will produce a circularly symmetric image whose radial intensity distribution, $h(r)$, may be readily computed.

Making use of the Fourier transform convolution theorem, we can write

$$H(\rho) = G(\rho) \cdot F(\rho) \quad (A-3)$$

where capitalization of the functions indicates their zeroth order Hankel transforms, and the variable ρ denotes spatial frequency. Explicitly, we have

$$F(\rho) = \frac{1}{[A\sigma_1^2 + B\sigma_2^2]} \cdot \left\{ A\sigma_1^2 \cdot \exp[-\pi^2 \sigma_1^2 \rho^2] + B\sigma_2^2 \cdot \exp[-\pi^2 \sigma_2^2 \rho^2] \right\}, \quad (\text{A-4})$$

and

$$G(\rho) = J_0(2\pi a \rho) \quad (\text{A-5})$$

where the symbol J_0 denotes the zeroth order Bessel function.

But, the radial intensity distribution of the image can be written

$$h(r) = 2\pi \int_0^\infty \rho H(\rho) J_0(2\pi r \rho) d\rho. \quad (\text{A-6})$$

Substituting equations (A-3), (A-4) and (A-5) into equation (A-6), we obtain

$$h(r) = \frac{2\pi}{[A\sigma_1^2 + B\sigma_2^2]} \left\{ A\sigma_1^2 \cdot T_1 + B\sigma_2^2 \cdot T_2 \right\}, \quad (\text{A-7})$$

where

$$T_k = \int_0^\infty \rho J_0(\alpha \rho) J_0(\beta \rho) \cdot \exp[-\theta_k^2 \rho^2] d\rho, \quad (\text{A-8})$$

where

$$\left. \begin{aligned} \alpha &= 2\pi a \\ \beta &= 2\pi r \\ \theta_k &= \pi \sigma_k \end{aligned} \right\}. \quad (\text{A-9})$$

Equation (A-8) is of a standard form tabulated by Gradshteyn and Ryzhik (1965). Explicitly, we have

$$T_k = \frac{1}{2\pi\sigma_k^2} \cdot \exp[-a^2/\sigma_k^2] \cdot \exp[-r^2/\sigma_k^2] \cdot I_0(2ar/\sigma_k^2) \quad (A-10)$$

where the symbol I_0 denotes the modified Bessel function of the first kind of zeroth order. Formulae for the computation of I_0 are given by Abramowitz and Stegun (1972).

ACKNOWLEDGMENTS

This research was supported by the National Aeronautics and Space Administration under contract NASW-3134 and grant NGR-03-003-001. The equipment used to gather the photometric data was developed, assembled, and tested with the support of National Science Foundation grants GP-6983 and GP-20090.

REFERENCES

- Abramowitz, M. and Stegun, I.A. (1972), "Handbook of Mathematical Functions," Dover: New York.
- Fink, U. and Larson, H.P. (1979), "The Infrared Spectra of Uranus, Neptune, and Titan From 0.8 to 2.5 Microns," *Astrophys. J.* 233 (In press).
- Freeman, K.C. and Lynga⁰, G. (1970), "Data for Neptune From Occultation Observations," *Astrophys. J.* 160, pp. 767-780.
- Giver, L.P.⁰ (1978), "Intensity Measurements of the CH₄ bands in the Region 4350Å to 10,600Å," *J. Quant. Spectrosc. Radiat. Transfer*, 19, pp. 311-322.
- Gradshteyn, I.S. and Ryzhik, I.M. (1965), "Tables of Integrals, Series, and Products," Fourth Edition, Prepared by Yu. V. Geronimus and M. Yu. Tseytlin, Translation Ed. A. Jeffrey, Academic Press, New York.
- Joyce, R.R., Pilcher, C.B., Cruikshank, D.P., and Morrison, D. (1977), "Evidence for Weather on Neptune I.," *Astrophys. J.* 214, pp. 657-662.
- Lockwood, G.W. (1978), "Analysis of Photometric Variations of Uranus and Neptune Since 1953," *Icarus* 35, pp. 79-92.
- Pilcher, C.B. (1977), "Evidence for Weather on Neptune II.," *Astrophys. J.* 214, pp. 663-666.
- Price, M.J. and Franz, O.G. (1976), "Limb Brightening on Uranus: The Visible Spectrum," *Icarus* 29, pp. 125-136.
- Price, M.J. and Franz, O.G. (1978), "Limb Brightening on Uranus: The Visible Spectrum II.," *Icarus* 34, pp. 355-373.
- Price, M.J. and Franz, O.G. (1979), "Uranus: Narrow-Waveband Disk Profiles in the Spectral Region 6000 to 8500 Angstroms," *Icarus* 38, pp. 267-287.
- Trafton, L. (1974), "Neptune: Observations of the H₂ Quadrupole Lines in the (4-0) Band," in *I.A.U. Symposium No. 65, "Exploration of the Planetary System,"* ed. A. Woszczyk and C. Iwaniszewska (Dordrecht: Reidel) pp. 497-512.

FIGURE CAPTIONS

- Figure 1. ⁰Stellar Slit Scans ($\lambda 6800\text{\AA}$): Comparison of Calculation with Observation. Composite observational data are illustrated by the solid curve. The best-fitting analytical curve is illustrated by the broken curve. The slit width was 0.645 arc. sec. The sample interval was 0.032 arc. sec.
- Figure 2. ⁰Stellar Slit Scans ($\lambda 7300\text{\AA}$): Comparison of Calculation with Observation. Composite observational data are illustrated by the solid curve. The best-fitting analytical curve is illustrated by the broken curve. The slit width was 0.645 arc. sec. The sample interval was 0.032 arc. sec.
- Figure 3. Model Neptune Slit Scans. Theoretical Scans were computed for each of the six models listed in Table II. The Neptune disk was taken to be circularly symmetric with an apparent angular radius of 1.168 arc. sec. Atmospheric smearing was described by the mean point spread function discussed in the text. The slit width was 0.645 arc. sec. All slit scans were normalized to equal total energy, obtained by integrating over the disk of the planet. Broadening and flattening of the slit scans increases progressively with the degree of limb-brightening on the disk.
- Figure 4. ⁰Neptune Slit Scans ($\lambda 6800\text{\AA}$): Comparison of Theory with Observation. Composite observational data are illustrated by the individual dots. The sample interval was 0.032 arc. sec. Theoretical scans, computed both for a uniform disk and for a ring of infinitesimal width, are illustrated by the solid curves. The Neptune disk was taken to be circularly symmetric with an apparent angular radius of 1.168 arc. sec. Atmospheric smearing was described by the relevant point spread function discussed in the text. The slit width was 0.645 arc. sec. All slit scans, both observational and theoretical, were normalized to equal total energy, obtained by integrating over the disk of the planet.
- Figure 5. ⁰Neptune Slit Scans ($\lambda 7300\text{\AA}$): Comparison of Theory with Observation. Composite observational data are illustrated by the individual dots. The sample interval was 0.032 arc. sec. Theoretical scans, computed both for a uniform disk and for a ring of infinitesimal width, are illustrated by the solid curves. The Neptune disk was taken to be circularly symmetric with an apparent angular radius of 1.168 arc. sec. Atmospheric smearing was described by the relevant point spread function discussed in the text. The slit width was 0.645 arc. sec. All slit scans, both observational and theoretical, were normalized to equal total energy, obtained by integrating over the disk of the plant.

between two oppositely wound coils of the QRS inductor. To renormalize the oscillator's mass m one might attach to it a conducting plate that resides in the inductor's magnetic field. The velocity of the plate through the magnetic field would induce an electric dipole moment on the plate which, in turn, would couple by its velocity to the magnetic field giving an interaction energy proportional to $\hat{p}^2 \hat{x}^2$ and thence a mass renormalization.

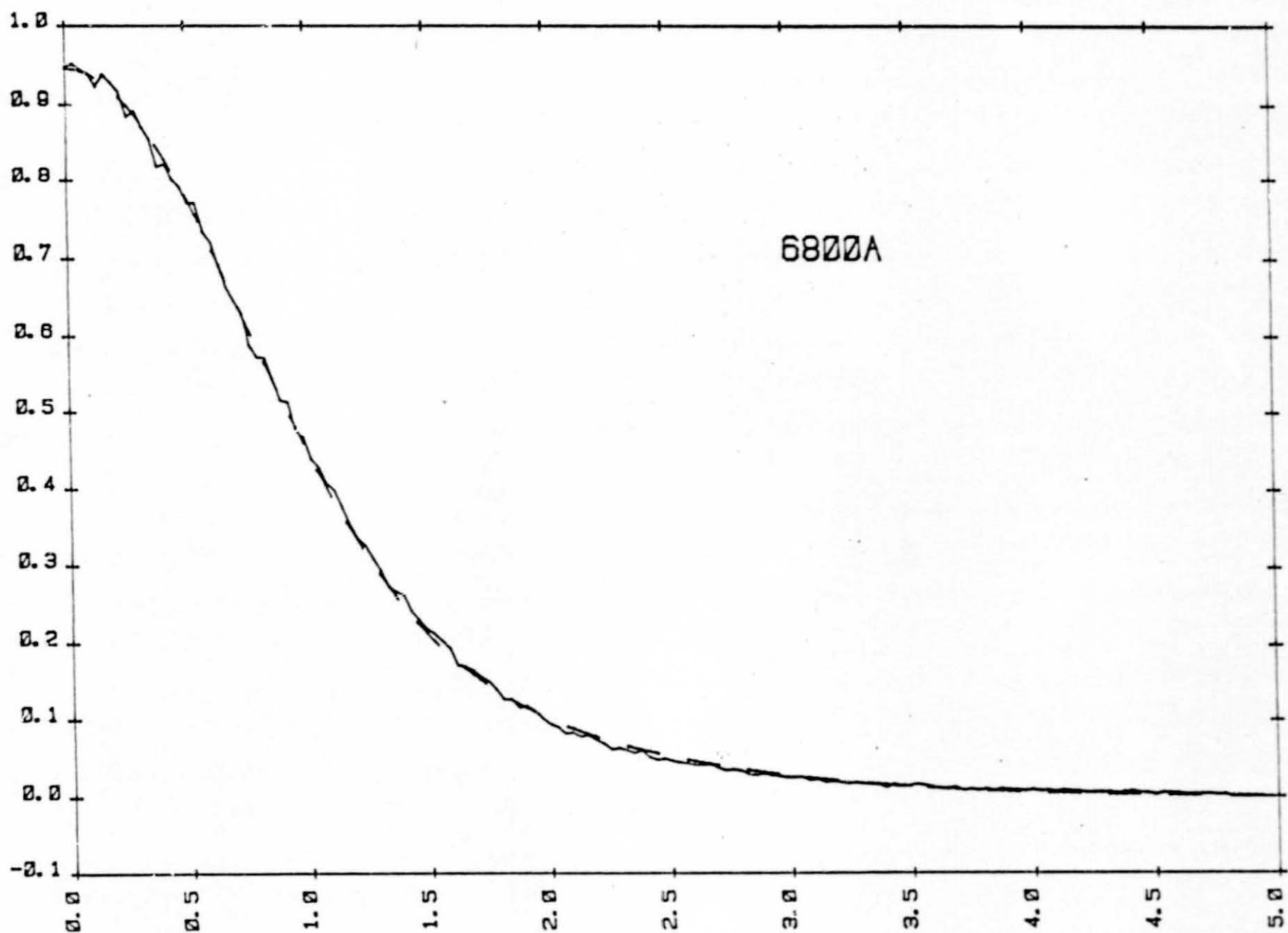
Unfortunately, these various ideas have not yet produced a viable design for clean coupling of a mechanical oscillator's energy \hat{H}_0 to a QRS. On the other hand, designs without clean coupling can still yield measurements of \hat{H}_0 more accurate than the amplitude-and-phase quantum limit $(n_0 + \frac{1}{2})^{\frac{1}{2}} \hbar \omega$. An example is a QRS that couples only to \hat{x}^2 , but that averages \hat{x}^2 over a number of cycles before sending it into the first classical stage (amplifier) (9,11). The measurement scheme of Fig. 1 will do this if the period of the circuit's (QRS) oscillations is much longer than the period of the mechanical oscillations. Then the circuit's capacitance (Eq. (24)) and resonant frequency will be sensitive to the time average of \hat{x}^2 and thence to \hat{H}_0 , with only small admixtures of sensitivity to the time-varying part of \hat{x}^2 and thence to the oscillator's phase $\hat{\psi}$. This is equivalent to the statement in Eq. (6) that $\hat{Q}_R = f(\hat{H}_0 + \alpha \langle \hat{H}_0 \rangle \hat{\psi})$ with $\bar{\alpha} \ll 1$, which in turn permits accuracies much better than $\Delta E = (n_0 + \frac{1}{2})^{\frac{1}{2}} \hbar \omega$. Reference (11) sketches a detailed analysis of this type of scheme, but for an electromagnetic oscillator with a mechanical QRS and with $\hat{H}_I = K \hat{x}^2 \hat{q}$ rather than $K \hat{x}^2 \hat{q}^2$ as in Fig. 1 and Eq. (24). That analysis reveals a limiting sensitivity

$$\Delta E \geq (n_0 + \frac{1}{2})^{\frac{1}{2}} (\Omega/\omega)^{\frac{1}{2}} \hbar \omega, \quad (25a)$$

where $E = (n_0 + \frac{1}{2}) \hbar \omega$ is the oscillator's energy, ω is its frequency, Ω is the frequency of the QRS, and $\Omega \ll \omega$. The corresponding limit on the

INTENSITY (ARBITRARY UNITS)

6800A



detection of a classical force $F_0 \cos(\omega t + \varphi)$, which drives changes in the oscillator's energy, is

$$F_0 \gtrsim \frac{2}{\tau} \left(\frac{m\omega\hbar}{\omega/\Omega} \right)^{\frac{1}{2}} \quad (25b)$$

if $\omega/\Omega < n_0 + \frac{1}{2}$. If $\omega/\Omega > n_0 + \frac{1}{2}$, then the limit (25a) on ΔE gets replaced by $\hbar\omega$, the ultimate precision with which one can ever measure energy changes; and correspondingly the force limit (25b) gets replaced by (21).

In measurements of the time average of \hat{x}^2 and thence \hat{n}_0 , it is not essential that the interaction Hamiltonian \hat{H}_I involve \hat{x}^2 . Instead \hat{H}_I can be proportional to \hat{x} , and then the internal workings of the QRS can produce the average of \hat{x}^2 at the entrance to the first classical stage.

BACK-ACTION-EVADING MEASUREMENTS OF \hat{X}_1

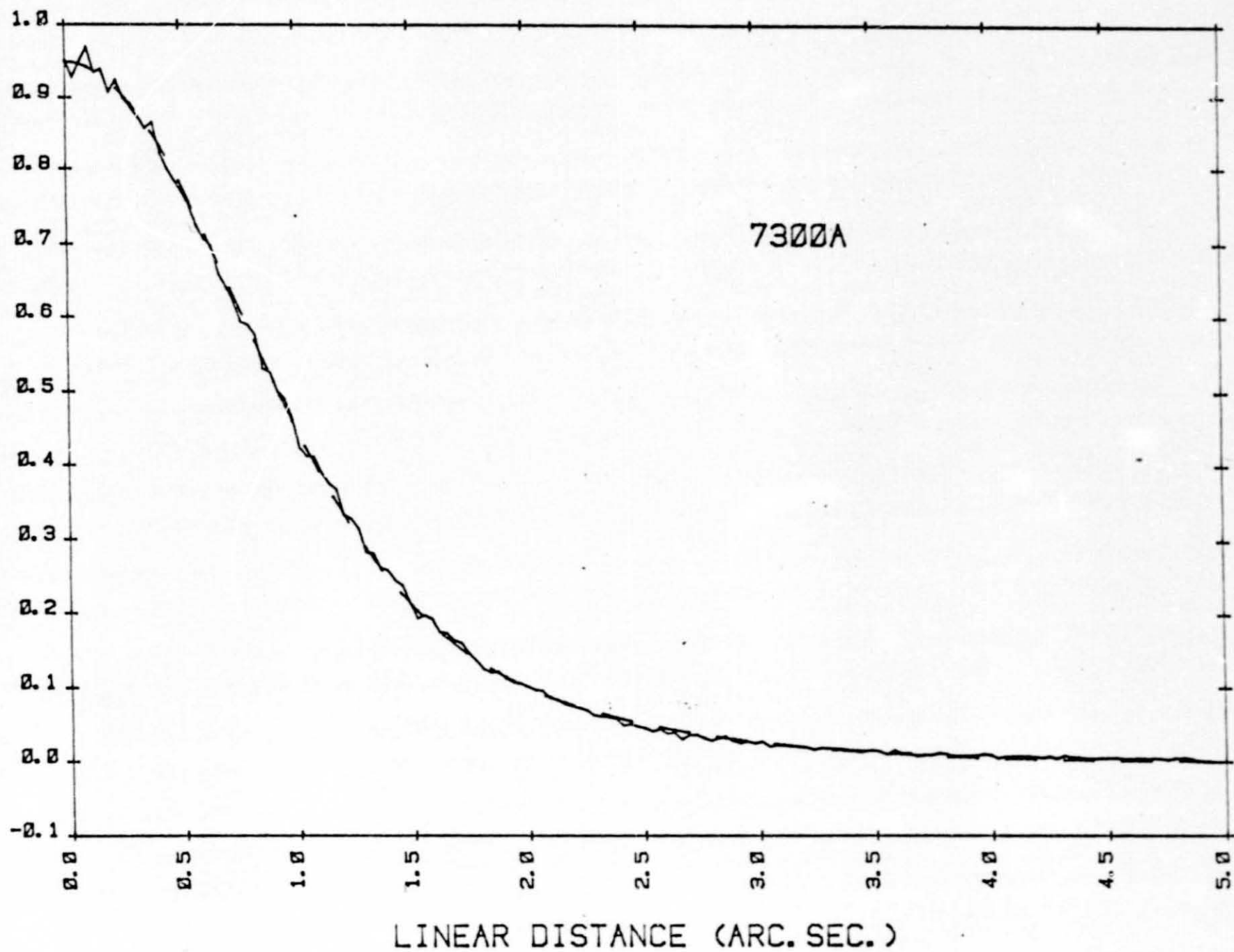
The QNDF observable $\hat{X}_1 = \hat{x} \cos \omega t - (\hat{p}/m\omega) \sin \omega t$ (real part of complex amplitude; Eq. (5)), like the position \hat{x} , has a continuous spectrum of eigenvalues; and in principle it can be measured arbitrarily quickly and accurately (13,15). Suppose that an initial "state-preparation" measurement at $t = 0$ has put the oscillator into an eigenstate $|\xi_0\rangle$ of $\hat{X}_1(0)$ with eigenvalue ξ_0 . A classical force $F(t)$ [total Hamiltonian $\hat{H} = \hat{H}_0 - \hat{x} F(t)$] will change \hat{X}_1 as seen in the Heisenberg Picture

$$\hat{X}_1(t) = \hat{X}_1(0) - \int_0^t [F(t')/m\omega] \sin \omega t' dt' . \quad (26)$$

In the Heisenberg Picture the oscillator's state remains fixed in time at $|\xi_0\rangle$, but this is an eigenstate of $\hat{X}_1(t)$ with eigenvalue

$$\xi(t) = \xi_0 - \int_0^t [F(t')/m\omega] \sin \omega t' dt' . \quad (27a)$$

INTENSITY (ARBITRARY UNITS)



Subsequent perfect measurements of \hat{X}_1 must yield this eigenvalue and will reveal the full details of its evolution. It evolves in exactly the same manner as X_1 would evolve for a classical oscillator (13,15).

One pays the price, in these measurements, of not knowing anything about the imaginary part of the complex amplitude \hat{X}_2 (Eq. (5c)). However, if one has a second oscillator coupled to the same force $F(t)$, one can measure the imaginary part \hat{Y}_2 of its complex amplitude, giving up all information about the real part \hat{Y}_1 . One's measurements must give the eigenvalue

$$\eta(t) = \eta_0 + \int_0^t [F(t')/m\omega] \cos \omega t' dt', \quad (27b)$$

which evolves in exactly the same manner as the X_2 or Y_2 of a classical oscillator. From the output of either oscillator, or better from the two outputs, one can deduce all details of the evolution of $F(t)$, no matter how weak $F(t)$ may be (13,15). Thus, \hat{X}_1 and \hat{Y}_2 are QNDF observables.

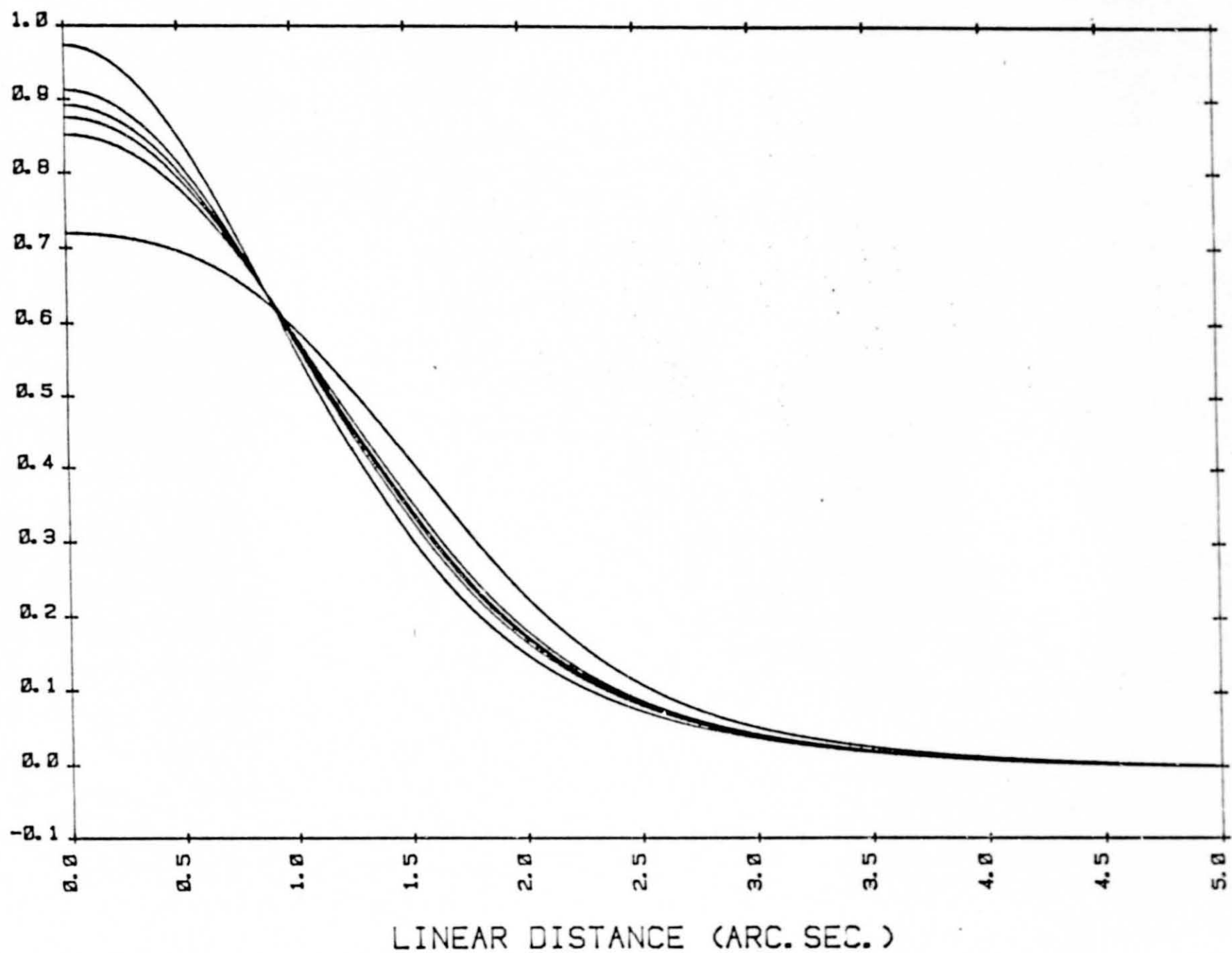
A perfect measurement of \hat{X}_1 (or \hat{Y}_2) requires (i) that the interaction Hamiltonian \hat{H}_I depend on \hat{X}_1 , and (ii) that \hat{H}_I commute with \hat{X}_1 (Eq. (7) and associated discussion). The simplest example is

$$\hat{H}_I = K \hat{X}_1 \hat{q} = K \hat{x} \hat{q} \cos \omega t - (K/m\omega) \hat{p} \hat{q} \sin \omega t. \quad (28)$$

A coupling of this type can be achieved, for a mechanical oscillator, by using a capacitive position transducer with sinusoidally modulated coupling constant ($\hat{H}_I = K \hat{x} \hat{q} \cos \omega t$), followed by an inductive momentum transducer with modulated coupling constant ($H_I = -(K/m\omega) \hat{p} \hat{q} \sin \omega t$). The two transducers together produce a voltage output

$$\hat{V} = \partial \hat{H}_I / \partial \hat{q} = K \hat{x} \cos \omega t - (K/m\omega) \hat{p} \sin \omega t = K \hat{X}_1, \quad (29)$$

INTENSITY (ARBITRARY UNITS)



which drives an electromagnetic circuit, the QRS, in which the charge \hat{q} flows (15). While capacitive position transducers and inductive velocity transducers are easy to construct, inductive momentum transducers are not. The momentum and velocity of the oscillator are related by

$$\dot{x} = \partial(H_0 + H_I)/\partial p = p/m - (K/m\omega) q \sin \omega t, \quad (30a)$$

which means that the classical Lagrangian $L = p\dot{x} - (H_0 + H_I)$ for oscillator-plus-transducers is

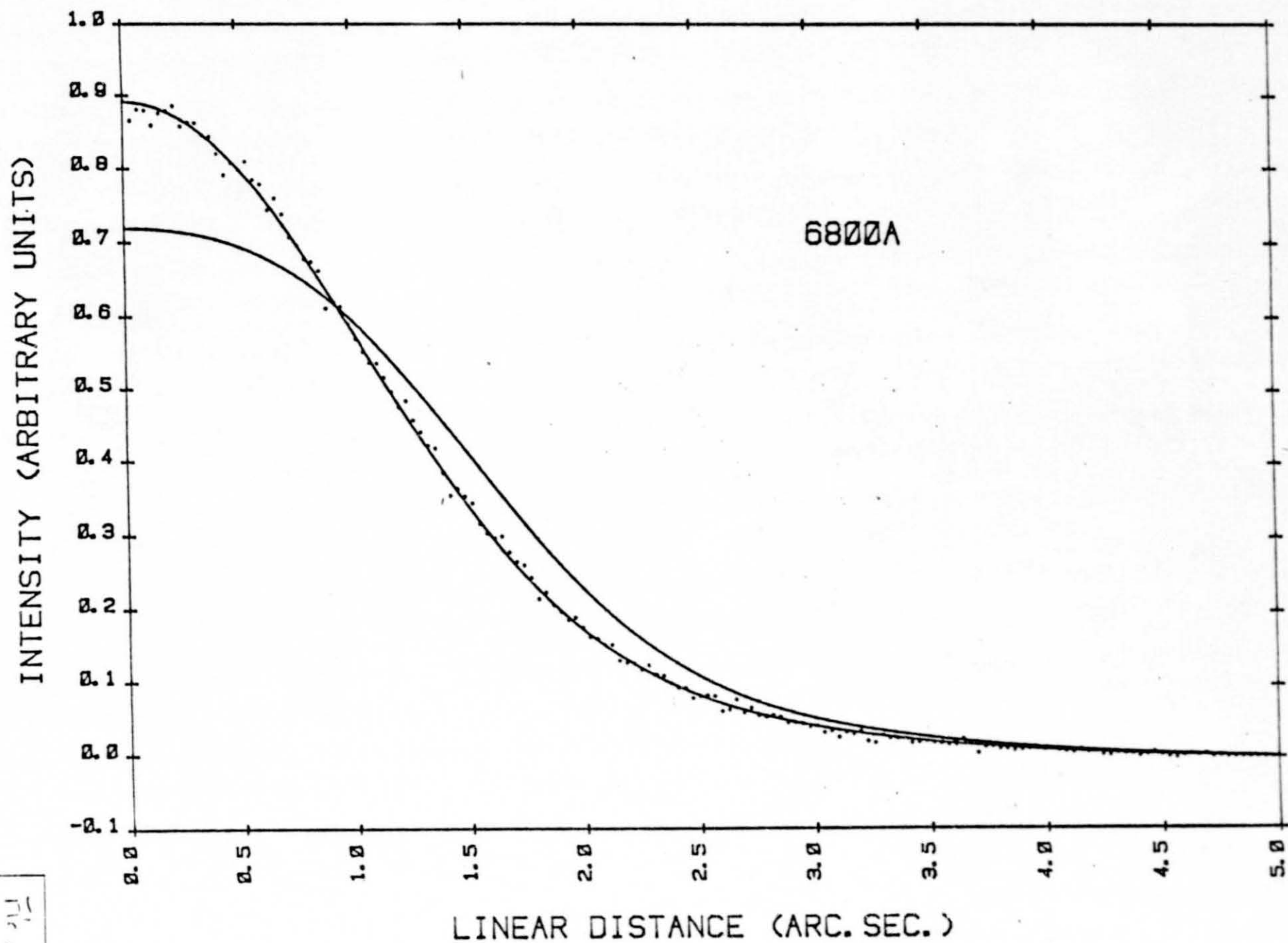
$$L = \frac{1}{2} m \dot{x}^2 - \frac{1}{2} m \omega^2 x^2 - K x q \cos \omega t + (K/\omega) \dot{x} q \sin \omega t + \frac{1}{2} m (K \sin \omega t / m \omega)^2 q^2. \quad (30b)$$

The first two terms represent the oscillator; the third is the capacitive position transducer; the fourth is an inductive velocity transducer (wire, physically attached to oscillator, moves through external magnetic field); and the last is a negative capacitor in the QRS circuit. Thus, an inductive momentum transducer is equivalent to an inductive velocity transducer (easy to construct) plus a negative capacitor (hard) (15). Although negative capacitors are not standard electronic components, they can be constructed in principle, and in principle they can be noise free (15).

For an electromagnetic oscillator with mechanical QRS, one can achieve the desired $\hat{H}_I = K \hat{\phi}_I \hat{q}$ using a capacitive transducer for the oscillator's "position" \hat{x} (\equiv charge in oscillator's capacitor) and an inductive transducer for its "momentum" \hat{p} (\equiv flux in oscillator's inductor). The momentum transducer turns out to involve a standard mechanical current transducer (current $\equiv \dot{x}$) plus a negative spring in the QRS (15). In principle negative springs can be noise free (15).

The sinusoidal modulations required in the transducers must be regulated by an external, classical clock, which has the same frequency ω as one's

Fig. 4



oscillator. One cannot use the oscillator itself as one's clock because in extracting the required oscillatory information from the oscillator one will produce an unacceptably large back action on \hat{X}_1 . However, before the experiment begins one can check the frequency of one's clock against that of the oscillator. In principle they can be made to agree perfectly, and in principle the clock can be made fully classical so its outputs are real numbers, $\cos \omega t$ and $\sin \omega t$, rather than operators (10,15). In practice, frequency drifts and quantum features of the clock need not cause serious experimental problems (15,20).

A perfect measurement of \hat{X}_1 , which lasts a finite time $\tilde{\tau}$, requires infinitely strong coupling in the transducers ($K \rightarrow \infty$) in order to give a signal that overwhelms zero-point noise in the QRS. If one has only finite coupling, then the zero-point noise accompanying the signal gives rise to a limit (Eqs. (16) and (17) with $x \rightarrow X_1$ and $N\tau \rightarrow \tilde{\tau}$) (Refs. (13-15))

$$\Delta X_1 \gtrsim (\hbar/2m\omega)^{\frac{1}{2}} (\beta\omega\tilde{\tau})^{-\frac{1}{2}}. \quad (31)$$

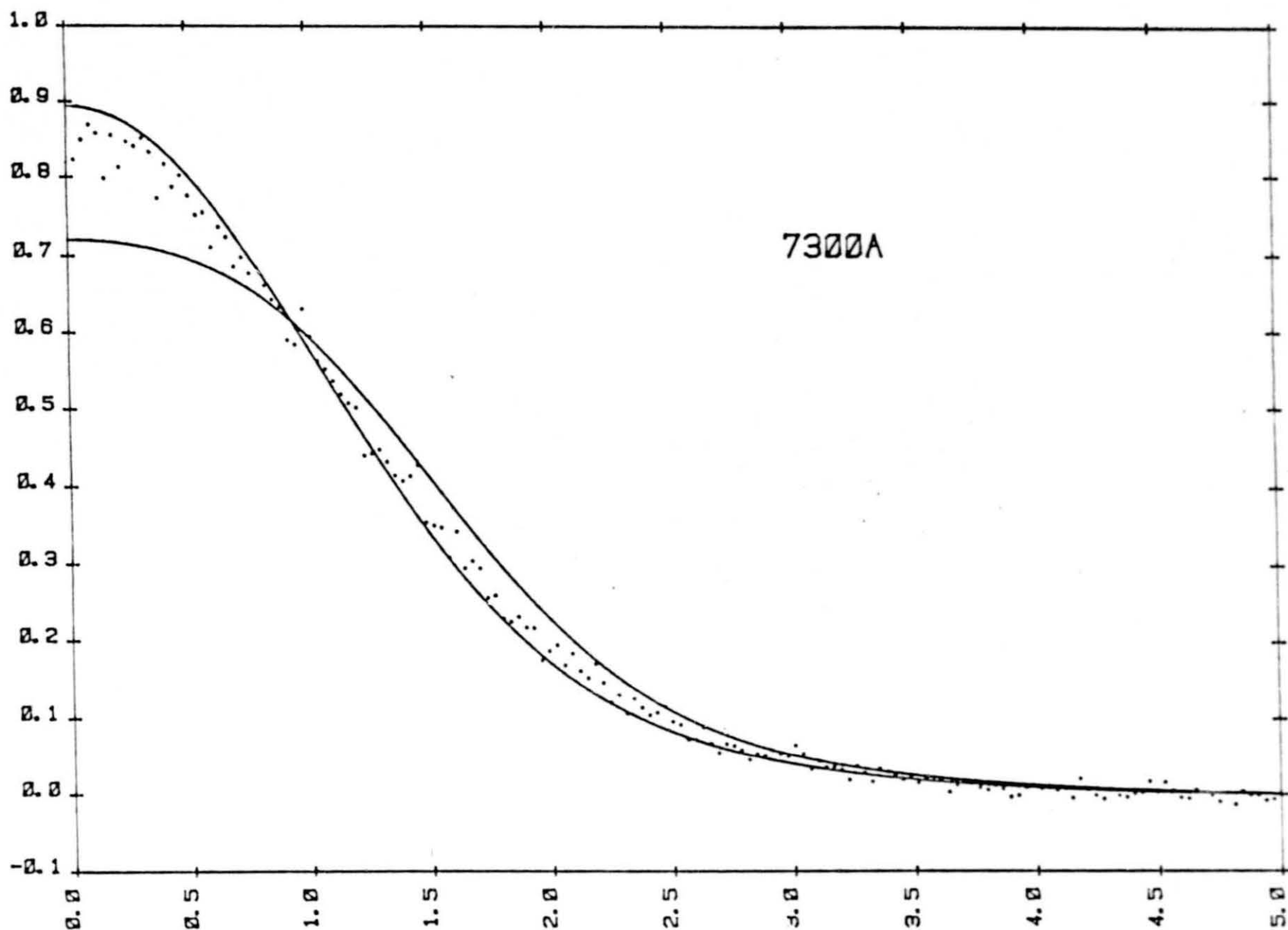
Here β is the dimensionless coupling constant (Eqs. (16)). Thus, whereas stroboscopic measurements with limited coupling can beat the amplitude-and-phase limit by a factor of only $(\beta\omega\tilde{\tau})^{-\frac{1}{4}}$ (Eq. (18b) with $N = \omega\tilde{\tau}/\pi$), continuous back-action-evading measurements of X_1 can beat it by $(\beta\omega\tilde{\tau})^{-\frac{1}{2}}$. Stroboscopic measurements are worse because of their smaller duty cycle.

In the realistic case of weak coupling, $\beta < 1$, one must average over many cycles ($\omega\tilde{\tau} \gg 1/\beta$) in order to substantially beat the amplitude and phase limit. In this case one can make use of a "trick" analogous to measuring the energy by coupling to \hat{x}^2 and averaging: One can perform a "single-transducer, back-action-evading measurement" (13,14,15) by coupling to

$$\hat{x} \cos \omega t \cos \Omega t = \frac{1}{2} (X_1 + X_1 \cos 2\omega t + X_2 \sin 2\omega t) \cos \Omega t \quad (32)$$

INTENSITY (ARBITRARY UNITS)

7300A



LINEAR DISTANCE (ARC. SEC.)

(i.e., $\hat{n}_I = 2K \hat{x} \hat{q} \cos \omega t \cos \Omega t$) and then sending the signal through a filter (the QRS) with bandpass at frequency $\Omega \gg \omega$ and bandwidth $\Delta f = 1/2\tau_* \ll \omega/2\pi$. The filter will "average the X_2 signal away" until its amplitude has fallen by $1/2\omega\tau_*$ relative to that of the X_1 signal. Since the initial rms X_2 signal strength is $1/\sqrt{2}$ that of the X_1 , this corresponds to $\hat{Q}_R = f(\hat{X}_1 + \hat{X}_2/2\sqrt{2}\omega\tau_*)$ in Eq. (6a), which together with the uncertainty relation (5c) and the argument of Eqs. (6) tells us that (20)

$$\Delta X_1 \gtrsim (\hbar/2m\omega)^{\frac{1}{2}} (2\sqrt{2}\omega\tau_*)^{-\frac{1}{2}}. \quad (33)$$

This is the error in X_1 due to back action from measurement of X_2 . The additional error due to zero-point noise accompanying the X_1 signal into the amplifier is (Eqs. (16) and (17) with $x \rightarrow X_1$ and $N\tau \rightarrow \tilde{\tau}$) (Refs. (14), (20))

$$\Delta X_1 \gtrsim (\hbar/2m\omega)^{\frac{1}{2}} (\beta\omega\tilde{\tau})^{-\frac{1}{2}}. \quad (34)$$

Here $1/2\tilde{\tau}$ is the bandwidth of the experiment ($\tilde{\tau}$ is the larger of the QRS averaging time τ_* , and the averaging time in subsequent electronics). The ultimate quantum limit on the sensitivity is (33) if $\beta > 2\sqrt{2}\tau_*/\tilde{\tau}$, and (34) if $\beta < 2\sqrt{2}\tau_*/\tilde{\tau}$. Note that Eq. (34) is the same limit (to within factors of order unity) as in the case of exact coupling to $\hat{X}_1 = \hat{x} \cos \omega t - (\hat{p}/m\omega) \sin \omega t$. Thus, when $\beta < 2\sqrt{2}\tau_*/\tilde{\tau}$ and $\omega\tilde{\tau} \gg 1$, one can abandon the momentum transducer without any serious loss of accuracy!

This type of single-transducer, time-averaged, back-action-evading measurement of X_1 appears today to be the most viable technique for beating the amplitude-and-phase limit (14) in gravitational-wave detection. In place of (14) one will face the limiting measurable force

$$F_0 \gtrsim (2/\tilde{\tau})(m\omega\hbar)^{\frac{1}{2}} \cdot \text{Max} \left[(\beta\omega\tilde{\tau})^{-\frac{1}{2}}, (2\sqrt{2}\omega\tau_*)^{-\frac{1}{2}} \right]. \quad (35)$$

THERMAL NOISE IN THE OSCILLATOR AND AMPLIFIER

The quantum limits derived above are not achievable in the laboratory today because thermal noise exceeds quantum mechanical noise.

Ignore for the moment thermal (Nyquist) noise in the oscillator. Then if the resistors in the QRS are cooled sufficiently, the dominant non-quantum noise will be that in the amplifier (first classical stage). The amplifier, which we assume to be linear, can be characterized by its power gain G and its noise temperature T_n . The QRS feeds the amplifier a signal at frequency $f = \Omega/2\pi$, to which the amplifier adds a noise power per unit bandwidth

$$\frac{dP_n}{df} = \frac{\hbar\Omega}{\exp(\hbar\Omega/kT_n) - 1} \quad (36)$$

Here k is Boltzmann's constant. If the incoming signal has power P_s , then the amplified signal and noise have power (23)

$$GP_s + \left(G \frac{\hbar\Omega}{\exp(\hbar\Omega/kT_n) - 1} + \frac{\hbar\Omega}{2} \right) \Delta f. \quad (37)$$

Here Δf is the bandwidth, and the $\hbar\Omega/2$ is a zero-point energy that accompanies the signal throughout its trek through the amplifier and other electronics, but does not get amplified (23). The quantum limits of previous sections of this article are attributable to this zero-point energy. In the presence of a real linear amplifier, with non-negligible noise temperature T_n , the signal power P_s must fight not $(\hbar\Omega/2)\Delta f$, but rather

$$\left(\frac{\hbar\Omega}{\exp(\hbar\Omega/kT_n) - 1} + \frac{1}{G} \frac{\hbar\Omega}{2} \right) \Delta f$$

(cf. Eq. (37)). Consequently, it is reasonable to expect that the

amplifier noise will modify our quantum limits (Eqs. (6c), (13)-(15), (17)-(19), (21), (22), (25), (31), (33)-(35)) by replacing \hbar with $\underline{(12)}$

$$\begin{aligned} \hbar + \frac{2kT_{\text{eff}}}{\Omega} &= \frac{2\hbar}{\exp(\hbar\Omega/kT_n) - 1} + \frac{\hbar}{G} \\ &= \frac{2kT_n}{\Omega} \quad \text{if } kT_n \gg \hbar\Omega \text{ and } G \gg 1. \end{aligned} \quad (38)$$

These modified quantum limits are sometimes called "amplifier limits". Quantum mechanical analyses of linear amplifiers (24,25) reveal a minimum possible noise temperature (noise temperature of "ideal linear amplifier")

$$\begin{aligned} (T_n)_{\min} &= \frac{\hbar\Omega}{k} \left[\ln \left(\frac{2 - 1/G}{1 - 1/G} \right) \right]^{-1} \\ &= \hbar\Omega/k \ln 2 \quad \text{if } G \gg 1, \end{aligned} \quad (39)$$

which is achievable in principle by a maser amplifier, and which corresponds to

$$(2kT_{\text{eff}}/\Omega)_{\min} = (2 - 1/G)\hbar. \quad (40)$$

Note that for large gains an ideal linear amplifier will give worse energy performance by a factor 2 ($\hbar \rightarrow 2\hbar$) than the quantum limits of previous sections.

The best linear amplifiers that have been built are parametric amplifiers and maser amplifiers, which operate at microwave frequencies and have (kT_{eff}/Ω) as small as $\sim 10 \hbar$. With such amplifiers one can only hope to get within a factor 10 or $\sqrt{10}$ of our quantum limits ($\hbar \rightarrow 10\hbar$). And to even achieve this one must design a QRS which upconverts the oscillator's signal frequency (kilohertz in the gravitational-wave case) to the microwave (gigahertz) region.

Any physical oscillator (e.g., the fundamental mode of a gravitational-wave bar antenna) is weakly coupled to a thermal bath of dynamical systems (e.g., sound waves in the bar). This coupling produces a frictional damping of large-amplitude motions, and it also produces a thermal-buffeting random walk of the oscillator's amplitude ("Nyquist noise"). The root-mean-square random-walk change of the oscillator's amplitude during time $\tilde{\tau}$ is

$$\begin{aligned} (\Delta x_0)_{\text{Nyq}} &= (\Delta p_0 / m\omega)_{\text{Nyq}} = (\Delta x_1)_{\text{Nyq}} = (\Delta x_2)_{\text{Nyq}} \\ &\simeq (kT / m\omega^2)^{\frac{1}{2}} (\omega\tilde{\tau} / Q)^{\frac{1}{2}}. \end{aligned} \quad (41a)$$

Here T is the temperature of the thermal bath (the bar's temperature), and Q is the oscillator's quality factor (number of radians of oscillation required for frictional damping of large-amplitude oscillations by a factor e in energy). The corresponding root-mean-square energy change is

$$(\Delta E)_{\text{Nyq}} \simeq (E_0 kT)^{\frac{1}{2}} (\omega\tilde{\tau} / Q)^{\frac{1}{2}}. \quad (41b)$$

These Nyquist noises must not exceed the amplifier limits (quantum limits with $\hbar \rightarrow 2kT_{\text{eff}}/\Omega$) if one is to achieve the amplifier limits in real experiments. Some numbers will be given below.

PROSPECTS FOR STROBOSCOPIC MEASUREMENTS

One possible scheme for stroboscopic measurements of a mechanical oscillator [gravitational-wave antenna with mass $m \simeq 10$ kg and frequency $\omega \simeq 3 \times 10^4 \text{ sec}^{-1}$] is shown schematically in Fig. 2. The mass of the oscillator is physically attached to the central, movable plate of a capacitor [(capacitance between outer plates) = C], which plays the role of transducer. The capacitor resides in the QRS — a high-frequency LC circuit [frequency $\Omega = (LC)^{-\frac{1}{2}} \simeq 10^{10} \text{ sec}^{-1}$], which has small losses [amplitude damping time $\tau = 2(RC\Omega^2)^{-1} \ll 0.1/\omega$] and

which is driven at its resonant frequency Ω by an external generator. In practice this circuit would be a microwave cavity; see Ref. (26). At the measurement times $\omega t = 0, \pi, 2\pi, \dots$ the generator is turned on for a time $\tau/2$ and then turned off, and in an additional time $\tau/2$ the excitations in the circuit die out. During the brief "on time" τ , the amplifier sees a voltage signal $V_s = (V_0/d) \Omega \tau x \cos \Omega t$, where V_0/d is the amplitude of the oscillating electric field between the capacitor plates. The experimenter averages the amplitude of this signal (with alternating sign) over N measurements to determine the position x of the oscillator.

It is straightforward to analyze the noise performance of this system using standard circuit theory. Alternatively, one can invoke the general formulas (15)-(19) for stroboscopic measurement schemes. Assuming that the resistor's physical temperature is less than the amplifier's effective temperature $T_{\text{eff}} \simeq 10$ K, the amplifier noise dominates and in Eq. (18b) we must replace $\hbar \rightarrow 2kT_{\text{eff}}/\Omega$. Assuming that the amplifier is properly impedance-matched to the circuit, the measurement will achieve the limiting precision (18b):

$$\Delta x \simeq \left(\frac{2kT_{\text{eff}}/\Omega}{m\omega} \right)^{\frac{1}{2}} (\beta N)^{-\frac{1}{4}}. \quad (42)$$

Comparison of the voltage signal with Eq. (16a) reveals that $K|g_{21}| = (V_0/\sqrt{2}d)(\Omega\tau)$; scrutiny of Fig. 2 reveals that the QRS output impedance, as seen by the amplifier, is $g_{22} = 2\tau/C$; consequently the dimensionless coupling constant of Eq. (16b) is $\beta = (V_0/d)^2 C\Omega\tau/(4m\omega^2)$. Combining this with the required pulse time $\tau = (\beta N\omega^2)^{-\frac{1}{2}}$ (Eq. (18a)), we find

$$\beta N = \left[\frac{(V_0/d)^2 C N \Omega}{4m\omega^3} \right]^{2/3}. \quad (43)$$

To avoid voltage breakdown in the capacitor, its electric-field amplitude should not exceed $(V_0/d) \simeq 10^6$ volts/cm. Assuming other reasonable parameters $C \simeq 1$ pf, $\Omega \simeq 10^{10}$ sec $^{-1}$, $N \simeq 1000$, $T_{\text{eff}} \simeq 10$ K, $m \simeq 10$ kg, $\omega \simeq 3 \times 10^4$ sec $^{-1}$, we find

$$\beta N \simeq 20, \quad \Delta x \simeq 1 \times 10^{-17} \text{ cm.} \quad (44)$$

Thus this system can achieve a sensitivity that is a factor $(20)^{\frac{1}{4}} \simeq 2.1$ below the "amplitude-and-phase" amplifier limit; but this is still an order of magnitude worse than the amplitude-and-phase quantum limit $(\hbar/2m\omega)^{\frac{1}{2}} \simeq 1 \times 10^{-18}$ cm.

Nyquist noise in the antenna (Eq. (41a) with $\omega\tilde{\tau} = \pi N$) will be less than the measurement precision $\Delta x \simeq 1 \times 10^{-17}$ cm if the antenna is cooled to 4 K and has a quality factor $Q \simeq 4 \times 10^9$. This is comparable to the best mechanical Q that has been achieved (27) for a sapphire crystal at 4 K.

PROSPECTS FOR SINGLE-TRANSDUCER BACK-ACTION-EVADING MEASUREMENTS

The configuration of Fig. 2 can also be used in a single-transducer, back-action evading measurement of \hat{X}_1 . In this case the circuit's amplitude damping time $2(RC\Omega^2)^{-1}$ becomes the averaging time τ_* of the QRS filter (previously it was the stroboscopic pulse length); and we require $\tau_* \gg 1/\omega$ (previously it was $\ll 1/\omega$). Instead of being pulsed, the generator's modulating voltage has the steady-state form $V_m = U_0 \sin \Omega t \sin \omega t$, which produces an electric field $(V_0/d) \cos \Omega t \cos \omega t$ in the capacitors ($V_0 = U_0 \Omega / 2\omega$). That electric field, interacting with the motions $x = X_1 \cos \omega t + X_2 \sin \omega t$ of the mechanical oscillator, produces a signal voltage

$$V_s = (V_0/d)(\Omega\tau_*/2) \left[X_1 \sin \Omega t + (2\omega\tau_*)^{-1} X_1 \sin \Omega t \sin 2\omega t - (2\omega\tau_*)^{-1} X_2 \sin \Omega t \cos 2\omega t \right] \quad (45)$$

at the output of the QRS. Amplification of this signal produces information about X_1 and X_2 with relative accuracies $\Delta X_1 = (2\sqrt{2}\omega\tau_*)^{-1} \Delta X_2$.

Assuming that the resistor noise is negligible compared to amplifier noise (which it will be for the parameters used below and for a resistor physical temperature $\lesssim T_{\text{eff}} \simeq 10^0 \text{K}$), we can compute the noise performance of this system from Eqs. (33), (34), and (16) with $\hbar \rightarrow 2kT_{\text{eff}}$. The best quality factor that has been achieved (26) for a superconducting microwave resonator (our QRS circuit) with a narrow capacitive gap is $Q_e = \Omega\tau_* \simeq 10^7$, corresponding to $\tau_* \simeq 10^{-3}$ sec. Consequently back-action forces (Eq. (33)) limit the sensitivity to

$$\Delta X_1 \simeq \left(\frac{kT_{\text{eff}}/\Omega}{m\omega} \right)^{\frac{1}{2}} \frac{1}{(2\sqrt{2}\omega\tau_*)^{\frac{1}{2}}} \simeq 2 \times 10^{-18} \text{ cm}, \quad (46)$$

a factor 7 below the amplitude-and-phase amplifier limit and approximately twice the amplitude-and-phase quantum limit. (Here we use $T_{\text{eff}} = 10^0 \text{K}$, $\Omega = 10^{10} \text{ sec}^{-1}$, $m = 10 \text{ kg}$, and $\omega = 3 \times 10^4 \text{ sec}^{-1}$ as before.) In order that Nyquist noise in the mechanical oscillator (Eq. (41a)) not exceed this sensitivity, the averaging time must not exceed $\tilde{\tau} \simeq 0.01 \text{ sec}$. (Here we use the same oscillator temperature and Q as before, $T = 4^0 \text{K}$ and $Q = 4 \times 10^9$.) To achieve the limit (46) we also require a coupling constant $\beta \simeq 2\sqrt{2}/\omega\tilde{\tau} \simeq 0.005$ (Eq. (34)). To compute β , first derive $K|g_{21}| = (V_o/d)(\Omega\tau_*/2\sqrt{2})$ from Eqs. (45) and (16a) with $x \rightarrow X_1$; then evaluate the impedance seen by the amplifier in Fig. 2 at the X_1 signal frequency $\Omega = (LC)^{-\frac{1}{2}}$, $g_{22} = 2\tau_*/C$; then evaluate Eq. (16b):

$$\beta = (V_o/d)^2 C\Omega\tau_*/(16m\omega^2). \quad (47)$$

The required β of 0.005 can be achieved with a reasonable electric field in

the capacitive gap: $V/d = 1 \times 10^5$ volts/cm.

This example and that of the last section confirm that it is easier to achieve a given level of sensitivity by continuous, single-sensor back-action evasion than by stroboscopic techniques. However, along the route toward realization of such experiments there remain a series of difficult experimental problems — not least of which is the frequency stability of the clock that regulates the voltage generator.

ON THE LIMITING FREQUENCY STABILITY OF A GENERATOR

Although current technology can achieve the frequency stability required by the above examples, it is of longer-term interest to know ultimate quantum mechanical limits on the stabilities of clocks.

At present the world's most stable clocks are the "superconducting cavity stabilized oscillator" (SCSO) (28) and the hydrogen maser (29). Both involve self-excited electromagnetic oscillations inside a cavity. In the SCSO the clock frequency Ω is regulated by the cavity's normal mode; and a change Δl of a typical dimension l of the cavity will produce a frequency change

$$\Delta\Omega/\Omega \simeq \Delta l/l. \quad (48)$$

In the maser, if the electromagnetic quality factor Q_e of the cavity (teflon bubble) exceeds $\frac{1}{2} \Omega \cdot (\text{mean time hydrogen atoms spend in cavity}) \equiv Q_a$, then expression (48) will be true. Otherwise, $\Delta\Omega/\Omega \simeq (\Delta l/l) \cdot (Q_e/Q_a)$, and the limit derived below is correspondingly modified.

Reference (30) derives a quantum limit on the frequency stability of any electromagnetic oscillator satisfying (48). The source of the limit is quantum fluctuations in the deformation of the cavity walls by electromagnetic

stresses. Since the stresses in the electromagnetic field are equal to its energy density \hat{H}_e/l^3 (with \hat{H}_e the Hamiltonian of the electromagnetic oscillator), the force on the walls is \hat{H}_e/l ; and this deforms the walls by $\delta l = \hat{H}_e/lk$ where k is the "mechanical spring constant" of the walls. The electromagnetic field is in a thermalized coherent state with n_0 quanta, which possesses quantum fluctuations $\Delta H_e \geq n_0^{-\frac{1}{2}} \hbar \Omega$; consequently, $\Delta l \geq n_0^{-\frac{1}{2}} \hbar \Omega / kl$, which leads to frequency fluctuations (Eq. (48))

$$\Delta \Omega / \Omega \geq n_0^{-\frac{1}{2}} \hbar \Omega / kl^2. \quad (49)$$

This "electromagnetic back-action" limit must be contrasted with the limiting precision for measurements of Ω during an averaging time $\tilde{\tau}$: $\Delta \Omega \geq \Delta \psi / \tilde{\tau}$, where $\Delta \psi \geq n_0^{-\frac{1}{2}}$ is the quantum uncertainty in the phase of the oscillator's coherent state:

$$\Delta \Omega / \Omega \geq n_0^{-\frac{1}{2}} (\Omega \tilde{\tau})^{-1} \quad (50)$$

("Townes-Schawlow limit"). These two limits lead to an optimal number of quanta n_0 , and an ultimate quantum limit

$$\frac{\Delta \Omega}{\Omega} \geq \left(\frac{\hbar}{kl^2 \tilde{\tau}} \right)^{\frac{1}{2}}. \quad (51)$$

For a cavity with wall thickness comparable to cavity dimensions l , or for a "cavity" made by coating the outside of a dielectric crystal with superconducting material (31), the spring constant k is related to the Young's modulus E_M of the cavity walls by $k \simeq E_M \cdot V / l^2$, where V is the cavity volume. Then

$$\Delta \Omega / \Omega \geq (\hbar / E_M V \tilde{\tau})^{\frac{1}{2}}. \quad (51')$$

In practice $E_M \lesssim 10^{13}$ dynes/cm, $V \simeq 1 \text{ cm}^3$, so $\Delta \Omega / \Omega \geq 10^{-20} \cdot (\tilde{\tau} / 1 \text{ sec})^{-\frac{1}{2}}$.

This limit is achievable in principle, but current technology is far from it.

Summary. Some future gravitational-wave antennas will be ~ 100 kilogram cylinders, whose end-to-end vibrations must be measured so accurately (10^{-19} centimeters) that they behave quantum mechanically. Moreover, the vibration amplitude must be measured over and over again without perturbing it ("quantum nondemolition measurement"). This contrasts with quantum chemistry, quantum optics, or atomic, nuclear, and elementary particle physics where one usually makes measurements on an ensemble of identical objects, and one cares not whether any single object is perturbed or destroyed by the measurement. This article describes the new electronic techniques required for quantum nondemolition measurements, and the theory underlying them. Quantum non-demolition measurements may find application elsewhere in science and technology.

REFERENCES AND NOTES

1. D. Bohm, Quantum Theory (Prentice Hall, Englewood Cliffs, NJ, 1951), esp. chapters 6 and 22.
2. W. Lamb, Physics Today, 22, 23 (1969).
3. Y. Aharonov and A. Peterson, in Quantum Theory and Beyond, T. Bastin, Ed. (Cambridge University Press, Cambridge, 1971), p. 135; and references cited therein.
4. C. W. Helstrom, Quantum Detection and Estimation Theory (Academic Press, New York, 1976).
5. V. B. Braginsky and V. N. Rudenko, Physics Reports, 46, 165 (1978).
6. J. A. Tyson and R. P. Giffard, Ann. Rev. Astr. Astrophys., 16, 521 (1978).
7. V. B. Braginsky and V. S. Nazarenko, Zhur. Eksp. Teor. Fiz., 57, 1421 (1969); English translation in Soviet Phys.—JETP, 30, 770 (1970).
8. V. B. Braginsky and Yu. I. Vorontsov, Uspekhi Fiz. Nauk, 114, 41 (1974); English translation in Soviet Phys.—Uspekhi, 17, 644 (1975).
9. W. G. Unruh, Phys. Rev. D, 18, 1764 (1978).
10. W. G. Unruh, Phys. Rev. D, 19, 2888 (1979).
11. V. B. Braginsky, Yu. I. Vorontsov, and F. Ya. Khalili, Zhur. Eksp. Teor. Fiz., 73, 1340 (1977); English translation in Soviet Phys.—JETP, 46, 705 (1977).
12. V. B. Braginsky, Yu. I. Vorontsov, and F. Ya. Khalili, Pis'ma Zhur. Eksp., Teor. Fiz., 27, 296 (1978); English translation in Soviet Phys.—JETP Letters, 27, 276 (1978).
13. K. S. Thorne, R. W. P. Drever, C. M. Caves, M. Zimmermann, and V. D. Sandberg, Phys. Rev. Letters, 40, 667 (1978).
14. K. S. Thorne, C. M. Caves, V. D. Sandberg, M. Zimmermann, and R. W. P. Drever, in Sources of Gravitational Radiation, L. Smarr, Ed. (Cambridge University Press, Cambridge, 1979).

15. C. M. Caves, K. S. Thorne, R. W. P. Drever, V. D. Sandberg, and M. Zimmermann, Rev. Mod. Phys., to be published January 1980.
16. J. N. Hollenhorst, Phys. Rev. D, in press.
17. L. I. Mandelstam, Complete Collected Works, Vol. 5 (1950).
18. V. B. Braginsky, Physical Experiments with Test Bodies (Nauka, Moscow, 1970); English translation published as NASA-TT F762 (National Technical Information Service, Springfield, VA).
19. R. P. Giffard, Phys. Rev. D, 14, 2478 (1976).
20. R. W. P. Drever, K. S. Thorne, C. M. Caves, M. Zimmermann, and V. D. Sandberg, paper in preparation.
21. G. W. Gibbons and S. W. Hawking, Phys. Rev. D, 4, 2191 (1971).
22. I. I. Gol'dman and V. D. Krivchenkov, Problems in Quantum Mechanics (Pergamon Press, London, 1961).
23. J. P. Gordon, in Quantum Electronics and Coherent Light, P. A. Miles, Ed. (Academic Press, New York, 1964), pp. 156-169.
24. J. Weber, Rev. Mod. Phys., 31, 681 (1959).
25. H. Heffner, Proc. IRE, 50, 1604 (1962).
26. V. B. Braginsky, V. I. Panov, V. G. Petnikov, and V. D. Popel'nyuk, Pribori Tekhnika Eksperimenta, 1, 234 (1977).
27. Kh. S. Bagdasarov, V. B. Braginsky, V. P. Mitrofonov, and V. S. Shiyon, Vestnik Moskovskogo Universiteta, Fiz. Astron., 18, 98 (1977).
28. S. R. Stein and J. P. Turneaure, IEEE Proceedings, 63, 1249 (1975).
29. R. F. C. Vessot, in Experimental Gravitation, B. Bertotti, Ed. (Academic Press, New York, 1974), p. 111.
30. V. B. Braginsky and S. P. Vyatchanin, Zhur. Eksp. Teor. Fiz., 74, 828 (1978); English translation in Soviet Phys.—JETP, 47, 433 (1978).
31. Kh. S. Bagdasarov, V. B. Braginsky, and P. I. Zubietov, Pis'ma Zhur. Tekh. Fiz., 3, 991 (1977).

32. For valuable discussions we thank C. M. Caves, R. W. P. Drever, and F. Ya. Khalili. For financial support we thank: (1) at Moscow University, the Ministry of Higher Education of the USSR; (2) at Caltech, the U.S. National Aeronautics and Space Administration [NGR 05-002-256 and a grant from PACE] and the U.S. National Science Foundation [AST76-80801 A92]; (3) for collaborative aspects of this work, the Cooperative Program in Physics between the National Academy of Sciences, USA and the Academy of Sciences, USSR, under the auspices of the USA-USSR Joint Commission on Scientific and Technological Cooperation [contract NSF-C310, Task Order 379].

FIGURE CAPTIONS

Fig. 1. A scheme for coupling a mechanical oscillator's (position)² $\equiv x^2$ to an electromagnetic QRS.

Fig. 2. A scheme for stroboscopic or continuous back-action-evading measurements of a mechanical oscillator. This scheme was devised independently in 1978 by V. B. Braginsky and by R. W. P. Drever, but has not previously been published.

Fig. 1

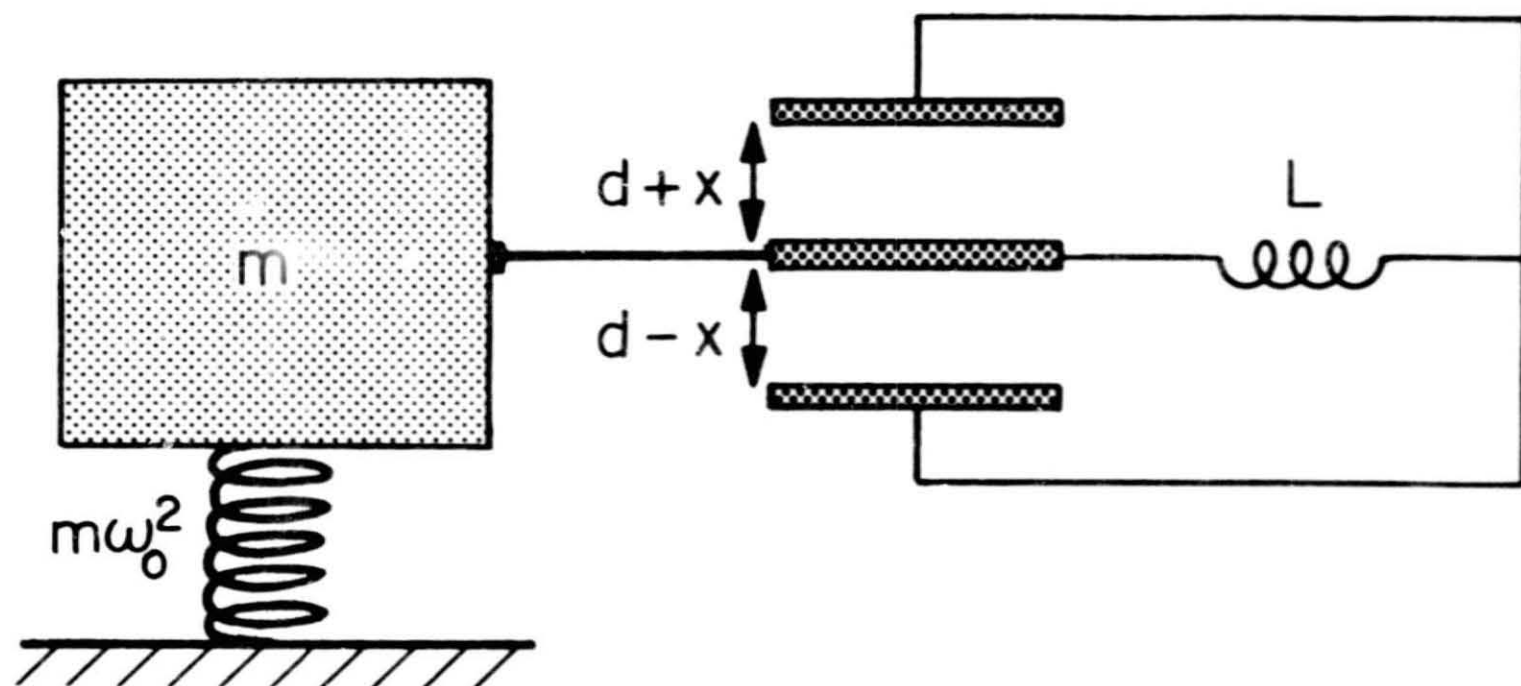


Fig. 2

